Hydrothermal synthesis of long-chain hydrocarbons up to C_{24} with $NaHCO_3$-assisted stabilizing cobalt

Daoping He[a,1], Xiaoguang Wang[a,1], Yang Yang[a], Runtian He[a], Heng Zhong[a,b,c,2], Ye Wang[d], Buxing Han[e,2], and Fangming Jin[a,b,c,2]

[a]School of Environmental Science and Engineering, State Key Laboratory of Metal Matrix Composites, Shanghai Jiao Tong University, Shanghai 200240, China; [b]Center of Hydrogen Science, Shanghai Jiao Tong University, Shanghai 200240, China; [c]Shanghai Institute of Pollution Control and Ecological Security, Shanghai 200092, China; [d]State Key Laboratory of Physical Chemistry of Solid Surfaces, Collaborative Innovation Center of Chemistry for Energy Materials, National Engineering Laboratory for Green Chemical Productions of Alcohols, Ethers, and Esters, College of Chemistry and Chemical Engineering, Xiamen University, Xiamen 361005, China; and [e]Beijing National Laboratory for Molecular Sciences, Key Laboratory of Colloid, Interface and Chemical Thermodynamics, Research/Education Center for Excellence in Molecular Sciences, Institute of Chemistry, Chinese Academy of Sciences, Beijing 100190, China

Edited by Donald Canfield, Institute of Biology, Syddansk Universitet, Odense, Denmark; received August 16, 2021; accepted November 3, 2021

Abiotic CO_2 reduction on transition metal minerals has been proposed to account for the synthesis of organic compounds in alkaline hydrothermal systems, but this reaction lacks experimental support, as only short-chain hydrocarbons (<C_5) have been synthesized in artificial simulation. This presents a question: What particular hydrothermal conditions favor long-chain hydrocarbon synthesis? Here, we demonstrate the hydrothermal bicarbonate reduction at ∼300 °C and 30 MPa into long-chain hydrocarbons using iron (Fe) and cobalt (Co) metals as catalysts. We found the Co^0 promoter responsible for synthesizing long-chain hydrocarbons to be extraordinarily stable when coupled with Fe−OH formation. Under these hydrothermal conditions, the traditional water-induced deactivation of Co is inhibited by bicarbonate-assisted CoO_x reduction, leading to honeycomb-native Co nanosheets generated in situ as a new motif. The Fe−OH formation, confirmed by operando infrared spectroscopy, enhances CO adsorption on Co, thereby favoring further reduction to long-chain hydrocarbons (up to C_{24}). These results not only advance theories for an abiogenic origin for some petroleum accumulations and the hydrothermal hypothesis of the emergence of life but also introduce an approach for synthesizing long-chain hydrocarbons by nonnoble metal catalysts for artificial CO_2 utilization.

abiotic synthesis | hydrothermal petroleum | long-chain hydrocarbon | carbon cycle | origin of life

Apart from the well-known microbial and thermogenic origin of hydrocarbons, the scenario of their abiogenic origin has emerged as an assumption and has been demonstrated on a few occasions (1, 2). Abiotic hydrocarbons production from inorganic carbon is considered to be driven by serpentinization in H_2-rich alkaline hydrothermal fluids, and, recently, the hydrocarbons generated are proposed to be transported through deep faults to shallower regions in the Earth's crust and contribute to some petroleum reserves (3). In addition, the current scenarios suggest that the abiotic synthesis of hydrocarbons in natural hydrothermal systems is also a potential source of prebiotic organic compounds for life's emergence (4). However, the mechanisms by which long-chain hydrocarbons are synthesized remains unclear and controversial because such reactions presently lack experimental support despite numerous artificial simulations of hydrocarbon formation, although short-chain hydrocarbons (<C_5) have been synthesized (5).

In general, the abiotic formation of hydrocarbons is assumed to proceed through the Fischer–Tropsch synthesis (FTS) pathway catalyzed by natural minerals (6, 7). The predominant, oxidized forms of dissolved carbon under high pressure, $CO_{2(aq)}$ or HCO_3^- (>70%), react with dissolved hydrogen $H_{2(aq)}$ to produce hydrocarbons. The process can be described as follows:

$$CO_{2(aq)} + [3 + (1/n)]H_{2(aq)} \rightarrow (1/n)C_nH_{2n+2} + 2H_2O, \quad [1]$$

$$HCO_3^- + [3 + (1/n)]H_{2(aq)} \rightarrow (1/n)C_nH_{2n+2} + 2H_2O + OH^-. \quad [2]$$

Fe(II) in the rock-forming minerals reduces H_2O to H_2, while the Fe(II) is converted to Fe(III) (8). In addition to Fe(II), as the H_2 electron donor, clues from biological mechanism and the chemical literature suggest that the native metals can act as the prebiotic source of electrons to fix CO_2 (9–13). The native Fe or the nickel–iron (awaruite, Ni_3Fe) and cobalt–iron (wairauite, CoFe; $CoFe_2$) alloys have been found in the Earth's serpentinized ultramafic rocks, where the occurrence of the cobalt–iron alloy is associated with iron minerals, such as chromite and awaruite (14–18). Thus, the native Fe, abundant natural Fe species, or its minerals combined with other transition metals are considered as promising reductants and/or catalysts to reduce CO_2 in hydrothermal systems were thermodynamic conditions to be far enough from equilibrium. To prove the hydrocarbon formation under geochemical conditions, many efforts have been made, and only short-carbon chains (≤C_5) can be produced from CO_2/HCO_3^-/CO_3^-, for example, with Fe–Cr oxide (chromite) (7) or awaruite (Ni_3Fe) in alkaline

Significance

The mechanisms by which abiotic, long-chain hydrocarbons are produced in natural alkaline hydrothermal systems are unknown, as only short-chain hydrocarbons (<5 carbons) have been experimentally observed to date. Here, we demonstrate how the hydrothermal reduction of bicarbonate into long-chain hydrocarbons (≤24 carbons) occurs through the use of iron and cobalt metals. In contrast to the traditional Fischer–Tropsch synthesis, in which water is the driving force for catalyst deactivation, Co exhibits unique catalytic stability in hydrothermal conditions through bicarbonate-assisted CoO_x reduction, thus promoting the carbon−carbon coupling process with the synergistic effect from the iron hydroxyl group. This finding helps to explain the abiogenic origin of petroleum, life's emergence, and further contributes to artificial carbon dioxide utilization in the chemical industry.

Author contributions: D.H. and F.J. designed research; D.H. and X.W. performed research; D.H., X.W., Y.Y., R.H., H.Z., Y.W., B.H., and F.J. analyzed data; and D.H. and F.J. wrote the paper.

The authors declare no competing interest.

This article is a PNAS Direct Submission.

See online for related content such as Commentaries.

[1]D.H. and X.W. contributed equally to this work.

[2]To whom correspondence may be addressed. Email: fmjin@sjtu.edu.cn, zhong.h@sjtu.edu.cn, or hanbx@iccas.ac.cn.

This article contains supporting information online at http://www.pnas.org/lookup/suppl/doi:10.1073/pnas.2115059118/-/DCSupplemental.

Published December 15, 2021.

CHEMISTRY

conditions (200 to ~400 °C, 40 to 50 MPa) (1) or with Fe-bearing dolomite (ankerite) at a higher temperature and pressure (600 to ~1,200 °C and 1 to ~6 GPa) (19). However, the long-chain hydrocarbons (>C_5) have not been formed, and it remains an open question as to how hydrothermal conditions might favor direct, long-chain hydrocarbon synthesis from CO_2/HCO_3^-/CO_3^-. Indeed, the lack of direct experimental evidence and mechanisms for long-chain hydrocarbon formation from CO_2/HCO_3^- in artificial alkaline hydrothermal systems has led to serious doubts regarding the supposed abiogenic origin of hydrocarbons, as well as the hypothesized evolutionary transition from geochemical to biochemical processes. Identifying hydrothermal settings that activate H_2–CO_2 redox reactions with a transition metal catalyst for long-chain hydrocarbon synthesis is an important step toward understanding prebiotic chemistry on the early Earth.

Additionally, the utilization of CO_2 as a feedstock for chemical fuel synthesis has received considerable research interest to reduce the carbon footprint and achieve a carbon-neutral cycle (20–22). Our previous efforts of hydrothermal CO_2 reduction with metals have shown that CO_2/HCO_3^- can be easily converted into C_1 products such as formate and methane (23, 24); however, it remains challenging to synthesize products beyond C_3, especially of long-chain hydrocarbons. In the traditional FTS performed with dry CO_2 gas and H_2, Co does exhibit catalytic activity for synthesizing long-chain hydrocarbons, yet it must be born in mind that Co is extremely unstable because of its easy oxidation when exposed to wet vapor (25–27). Moreover, the CoO_x formed is difficult to reduce, as the ambient water acts as an oxidant, thus deactivating the Co catalyst (28). Thus, this chemical engineering field has been left to the noble metal catalysts (29–31) or organic solvents (32), seriously limiting their applications. Recently, we found that a minor portion of the Co remained in the metallic phase during the hydrothermal reduction of CO_2 to acetate (33). Although the mechanism by which the portion of the Co phase remains under hydrothermal conditions is unknown, the phenomenon brought to mind the unique role of hydrothermal systems to stabilize the valence state of Co, thus making possible the synthesis of long-chain hydrocarbons.

Here, we report the hydrothermal synthesis of long-chain hydrocarbons with the use of metal Fe (as a reductant) and Co as a catalyst by designing a dynamic redox equilibrium system for maintaining Co stability. We demonstrate that CoO_x can be reduced via $CoCO_3$ in the presence of bicarbonate under hydrothermal conditions that inhibit Co deactivation in water, as honeycomb nanosheets are generated in situ as new motif. The unique stability and honeycomb nanosheets of Co coupled with the synergistic effect of Fe−OH and Co metal result in long-chain hydrocarbon formation (up to 24 carbons) from HCO_3^- reduction at ~300 °C and ~30 MPa. Such hydrothermal synthesis in a manner comparable to geochemical expectations of serpentinization of ultramafic rocks comprising the oceanic crust is of significance not only to the abiogenic origin of petroleum, the emergence of life, but also to the demonstration of how such hydrocarbons can be generated in the absence of noble metals of significance to the chemical industry.

Results and Discussion

$NaHCO_3$-Assisted Stabilization of Co. Although the existence of a minor Co metal phase was observed in our past research into the hydrothermal reduction of CO_2 to acetate, the mechanisms by which a portion of Co^0 was retained and stabilized in water remained unknown. Considering the actual oxidation of Co^0 in water, we surmise that the stability could be attributed to a dynamic equilibrium between oxidation and reduction during the hydrothermal reactions. The direct reduction of CoO_x under low temperature, such as 300 °C, is difficult. Thus, we first investigated whether, and how, CoO_x could be reduced under hydrothermal conditions. The alkaline hydrothermal environment involves the participation of dissolved carbon compounds, which may react with CoO_x and change the reaction pathway. Here, we conducted CoO reduction at 300 °C with H_2 gas as a function of time in alkaline hydrothermal conditions. The $NaHCO_3$ is selected as the carbon source to create alkaline conditions (pH ~8.23) (*SI Appendix*, Table S1), as it has been considered the dominant species among all the dissolved carbon species [$CO_{2(aq)}$, H_2CO_3, HCO_3^-, and CO_3^{2-}] in CO_2-saturated alkaline vent fluids (pH ~9) (1, 8, 34). In the presence of HCO_3^-, the CoO was quickly reduced to Co within 1 h (Fig. 1*A*), and a small amount of $CoCO_3$ was detected at a short reaction time of 0.5 h and a low temperature of 200 °C (Fig. 1 *A* and *B*). These results indicate that CoO can be reduced to Co^0 via a $CoCO_3$ intermediate. In contrast, in the absence of HCO_3^-, $Co(OH)_2$ was generated, and only a very small quantity of CoO was converted to Co. Thermodynamic calculation also demonstrated that the reduction of CoO via $CoCO_3$ intermediate is more favorable (Fig. 1*C*). Taken together, these results demonstrate that the presence of HCO_3^- not only promotes the reduction of CoO into Co^0 but, thereafter, keeps it stable under these hydrothermal, reducing conditions.

Hydrothermal Synthesis of Long-Chain Hydrocarbons by Co. After demonstrating the stability of metallic Co under hydrothermal conditions, we tested whether long-chain hydrocarbons could be synthesized by using $NaHCO_3$ as a carbon source, Fe as a reductant, and Co^0 as a catalyst. The reduction of $NaHCO_3$ was executed in a 42-mL stainless steel autoclave with a water-filling level of 50% at 200 to 300 °C and 20 to 30 MPa—approximating a natural hydrothermal environment (temperature of ≤400 °C and pressure of ≤100 MPa) (35–38). A control experiment was performed first using only Fe without Co, whereby only $HCOO^-$ and minor methane were obtained (*SI Appendix*, Table S2 and Fig. S1 and Fig. 2*A*). To our delight, the formation of long-chain hydrocarbons was clearly observed in the presence of metallic Co (Fig. 2), suggesting that Co^0 exhibited catalytic activity for C−C coupling. Moreover, increases in the concentration of $NaHCO_3$, as well as of the operating temperature of the system, led to a continually increasing hydrocarbon number, as to be expected of hydrocarbon production kinetics (*SI Appendix*, Fig. S2). Also, the high-$NaHCO_3$ concentration is found to enhance the oxidation of Fe (*SI Appendix*, Fig. S3), leading to the accumulation of in situ hydrogen and thereby concomitant high pressure forcing long-chain hydrocarbon formation. In contrast, on reducing the concentration of Fe and $NaHCO_3$ by half, the amount of short-chain hydrocarbons decreased, and the formation of long-chain hydrocarbons was not observed (*SI Appendix*, Table S2).

As shown in Fig. 2*A*, the products were dominated by a homologous series of linear alkanes (*SI Appendix*, Fig. S4) with carbon chains of up to 24 carbons. Relative to linear alkanes, small amounts of alkenes (*SI Appendix*, Figs. S5–S7) and branched alkanes (*SI Appendix*, Figs. S8–S11) were also detected (Fig. 2*B*). Alkenes are important feedstocks to generate macromolecules or chiral compounds by secondary reactions. More importantly, the linear alkanes exhibited a regular log-linear decrease in abundance with an increasing number of carbons in the alkyl chain, commonly referred to as an Anderson–Schulz–Flory distribution (Fig. 2*C*). The ethane and propane display a regular pattern of decreasing ^{13}C content with increasing carbon number but are all enriched in ^{13}C relative to methane (Fig. 2*D*), which is consistent with the results starting from CO/HCO_2^- using the FTS mechanism (36, 37). Thus, the structures and relative abundances of long-chain hydrocarbons generated closely resembled those of long-chain carbons produced by a typical FTS. The selectivity of C_2 to ~C_{24} reached 24%. Considering that the primary Co minerals

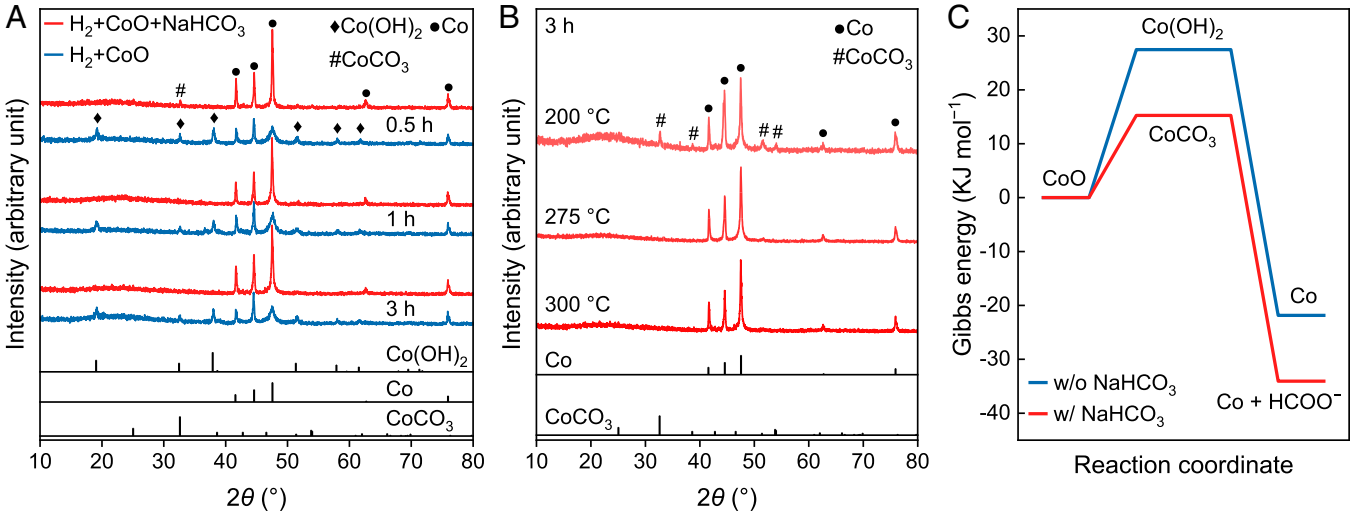

Fig. 1. $NaHCO_3$-assisted, hydrothermal CoO reduction. (*A*) Time-dependent XRD patterns of solid sample after hydrothermal reduction of CoO by H_2 at 300 °C in the presence (red lines) or absence (blue lines) of $NaHCO_3$. (*B*) Temperature-dependent XRD patterns of solid sample after hydrothermal reduction of CoO by H_2 for 3 h in the presence of $NaHCO_3$. Experimental conditions are the following: H_2, 5 MPa; $NaHCO_3$, 80 mmol; CoO, 40 mmol; water filling, 50%; pH ~8. The vertical black lines in *A* and *B* are the XRD peaks of standard $Co(OH)_2$ (JCPDS No. 30–0443), Co (JCPDS No. 01–1278), and $CoCO_3$ (JCPDS No. 11–0692). (*C*) Gibbs energy of CoO reduction via $Co(OH)_2$ and $CoCO_3$ pathway, respectively. JCPDS: Joint Committee on Powder Diffraction Standards.

of wairauite (CoFe) and $CoFe_2$ are generated during serpentinization in the Earth's ultramafic crust or upper mantle, the highest average cobalt content occurs in ultramafic rocks reaches a substantial ~110 ppm (14–18), and also considering the geochemically feasible environment in this study, the results demonstrated herein provide direct evidence for the possible abiotic formation of hydrocarbons in natural alkaline hydrothermal systems.

Morphological Evolution of Co. To further probe Co stabilization, the solid phase was analyzed by X-ray diffraction (XRD), as shown in *SI Appendix*, Fig. S12. The Co maintains its native valence state, while Fe is oxidized into magnetite (Fe_3O_4). Element-mapping (Fig. 3*G*) distribution also confirmed the existence of native Co and Fe oxide. Although Co maintains an unchanged valence state, interestingly, the morphology of Co changed completely. Initially, Co powder was used in the experiment (Fig. 3*A*), yet honeycomb Co nanosheets formed after a short reaction time of 10 to ~30 min (Fig. 3 *B* and *C*) and were clearly observed for a longer reaction time of 1 to ~3 h (Fig. 3 *D* and *E*). The change from the initial Co powder to the honeycomb nanosheets indicates that the native Co underwent oxidation (dissolution) and reduction (reprecipitation), resulting in no overall change in the valence state before and after the reaction, despite the change in morphology. As discussed before, although the reduction of CoO_x is difficult in industrial FTS, the hydrothermal reduction of CoO into Co is relatively readily reached through the assistance of HCO_3^-, thus stabilizing Co through redox equilibrium.

Moreover, the H_2 produced in situ from Fe oxidation may serve as a template to assemble the dissolved/exfoliated Co into honeycomb nanosheets. A control experiment was performed, in which ex situ H_2 instead of Fe was used. As expected, no honeycomb Co nanosheets were observed (Fig. 3*F*). Thus, the in situ–produced H_2 from Fe oxidation achieved multiple purposes: reducing $NaHCO_3$ into long-chain hydrocarbons, reducing CoO into Co to maintain the stability of Co, and acting as a template to assemble the dissolved/exfoliated Co into a honeycomb structure. Moreover, the number of long-chain hydrocarbons (C_6 to ~C_{21}) exhibited a sharp increase in the first 3 h (*SI Appendix*, Fig. S13), which was consistent with the formation of honeycomb nanosheets. These results clearly indicate that the formation of nanostructured Co accelerates C–C coupling. Also, the formation of long-chain hydrocarbons and nanosheets are not dependent on the initial Co morphology (*SI Appendix*, Fig. S14) and can be efficiently catalyzed by recycled Co–Fe_3O_4 (*SI Appendix*, Fig. S15).

We also experimented with different transition metals and metal oxides as catalysts at the same hydrothermal conditions, such as Ni, Cu, Mo, TiO_2, ZnO, and Al_2O_3, as additives (*SI Appendix*, Table S2) for abiotic synthesis because they may have occurred in the prebiotic alkaline hydrothermal fluids and constitute the main components of mineral deposits. The results show that only Co in the presence of Fe has the function to catalyze C–C coupling for long-chain hydrocarbon synthesis, demonstrating the irreplaceability of native Co as a catalyst that is also found in certain hydrogenations known from microbiological and chemical studies (39–41).

Mechanism of C–C Coupling to Long-Chain Hydrocarbons. We next attempted to elucidate the mechanism of long-chain hydrocarbon formation in our hydrothermal system. One important question was whether our synthesis of long-chain hydrocarbons followed the traditional mechanism of FTS (i.e., is $NaHCO_3$ first reduced to CO which only then undergoes further reduction to a hydrocarbon?). Our gas chromatography–mass spectrometry (GC-MS) analysis of the gas sample did show that CO was formed (*SI Appendix*, Fig. S16), and furthermore, operando-attenuated total reflectance Fourier transform infrared (ATR-FTIR) spectroscopy was developed (*SI Appendix*, Fig. S17) to confirm CO formation and the study of the mechanism. During heating, two peaks located at 2,128 and 1,935 cm^{-1}, clearly represented linear-type CO adsorbed on Co and Co–Fe interfacial sites, respectively (42–44). The gradual intensification of the peaks with increasing reaction temperature (Fig. 4*A*) also indicates the formation of CO. The experiment with CO as the initial carbon source for substituting $NaHCO_3$ under the same conditions also generated long-chain hydrocarbons (*SI Appendix*, Fig. S18). Thus, our hydrothermal $NaHCO_3$ reduction does follow a typical FTS mechanism via CO intermediate pathway.

However, the initial CO generated by $NaHCO_3$ reduction often reacted with OH^- to produce $HCOO^-$ under alkaline

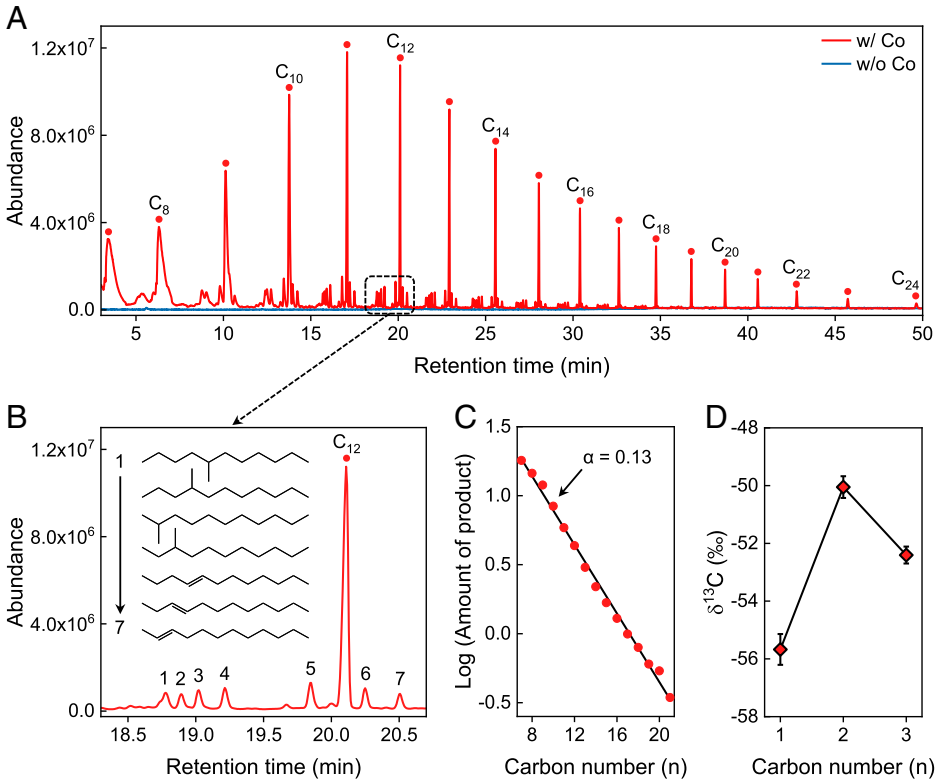

Fig. 2. Identification of hydrocarbons synthesized by the hydrothermal reduction of $NaHCO_3$. (*A*) Total ion chromatogram from GC-MS analysis of liquid products synthesized in the presence (red line) or absence (blue line) of Co. Experimental conditions are the following: Fe, 80 mmol; $NaHCO_3$, 80 mmol; Co, 40 mmol; water filling, 50%; 300 °C, 9 h, pH 8.23, 30 MPa. The number, n, in the C_n label indicates the carbon chain length of the linear alkanes (only even-numbered peaks are labeled). (*B*) Enlarged spectra of alkenes and branched alkanes of C_{12} compounds marked with the red square in *A*. (*C*) Abundances of linear alkanes generated under hydrothermal conditions. Lines are linear regressions of the C_7 to ~C_{21} alkanes, in which the chain growth probability (α) was 0.13. (*D*) Carbon isotopic composition of CH_4, C_2H_6, and C_3H_8.

hydrothermal conditions. Our current results and previous works also demonstrated that only $HCOO^-$ was formed when Fe alone was used. It is known that enhanced CO adsorption on Co is key for C−C coupling in FTS; thus, our results indicate that CO can be stabilized on the Co surface under alkaline hydrothermal conditions with the use of Fe.

We further probed how the CO was stabilized by operando ATR-FTIR. Two significant peaks at 3,676 and 3,226 cm^{-1}, attributed to the surface hydroxyl groups on Fe (Fe−OH) (42, 45, 46), appeared and intensified gradually with increasing reaction temperature (Fig. 4*A*). Surface hydroxyl groups have been proposed to interact with CO_2/CO to enhance the CO_2/CO adsorption strength (47, 48). The lower wavenumber of the CO_{ads} band (1,935 cm^{-1}) indicates the stronger adsorption of CO on the Co surface (49), which may be attributed to the role of the Fe−OH group, but to further confirm the role of Fe−OH, experiments replacing Fe with H_2 in the presence of Co were performed. In these cases, the formation of long-chain hydrocarbons was not observed, indicating that Co alone has no catalytic activity. Therefore, Fe or its oxidation/hydroxylation products are a crucial part of the reduction mechanism herein. Together with the detection of Fe−OH, this result suggests that the oxidation products of Fe should involve Fe−OH entities such as green rust (50). Moreover, the peak from the hydroxyl group in Fe−OH almost disappeared in the absence of Co (*SI Appendix*, Fig. S19), indicating that the formation of Fe−OH was promoted by Co.

Experiments were further conducted by changing the initial amount of Co to study its influence on the Fe−OH formation. The formation of siderite ($FeCO_3$) was observed in the absence of Co (Fig. 4*B*); however, the XRD peak intensity of $FeCO_3$ decreased with increasing amounts of Co, and the peak of $FeCO_3$ completely disappeared when the amount of Co reached 40 mmol. Moreover, the distribution of the products between hydrocarbons and $HCOO^-$ changed in response to the amount of Co catalyst (Fig. 4*C*). The formation of $HCOO^-$ gradually decreased with increasing amounts of Co, and the synchronized trend of $FeCO_3$ and $HCOO^-$, combined with the results of previous intensive studies (23), suggests that $FeCO_3$ is responsible for $HCOO^-$ formation. The formation of $FeCO_3$ and its reductive decomposition into HCOONa and Fe_3O_4 was thermodynamically favorable [$\Delta_r G^\theta$ (573 K) = −102.2 kJ · mol^{-1}].

In contrast, the number of long-chain hydrocarbons continued to increase with the Co amount (Fig. 4*C*). Therefore, the presence of Co reduced the formation of $HCOO^-$ and promoted the formation of hydrocarbons by suppressing the formation of $FeCO_3$ and promoting Fe oxidation via Fe−OH. The reason that Fe oxidation prefers to form $FeCO_3$ rather than proceed via the Fe−OH pathway in the absence of Co is because the formation of $Fe(OH)_x$ is thermodynamically less favorable [$\Delta_r G^\theta$ (573 K) > 12.9 kJ · mol^{-1} (x = 2)]. In the presence of Co, the formation of Fe−OH is attributed to the higher-adsorption energy of COOH on Co (−2.28 eV) (51) than that on FeO_x (−1.04 eV) (52), which promotes the transformation of the intermediate COOH reduced from $FeCO_3$ to the Co surface, leading to the formation of $Fe(OH)_x$.

Proposed Pathway of C−C Coupling versus $HCOO^-$. Based on the mechanism of C−C coupling, we propose a possible pathway of $NaHCO_3$ reduction to hydrocarbons using Fe and Co (Fig. 4*D*). First, HCO_3^- adsorbs on the surface of Fe because the formation of $FeCO_3$ is thermodynamically favorable, and the

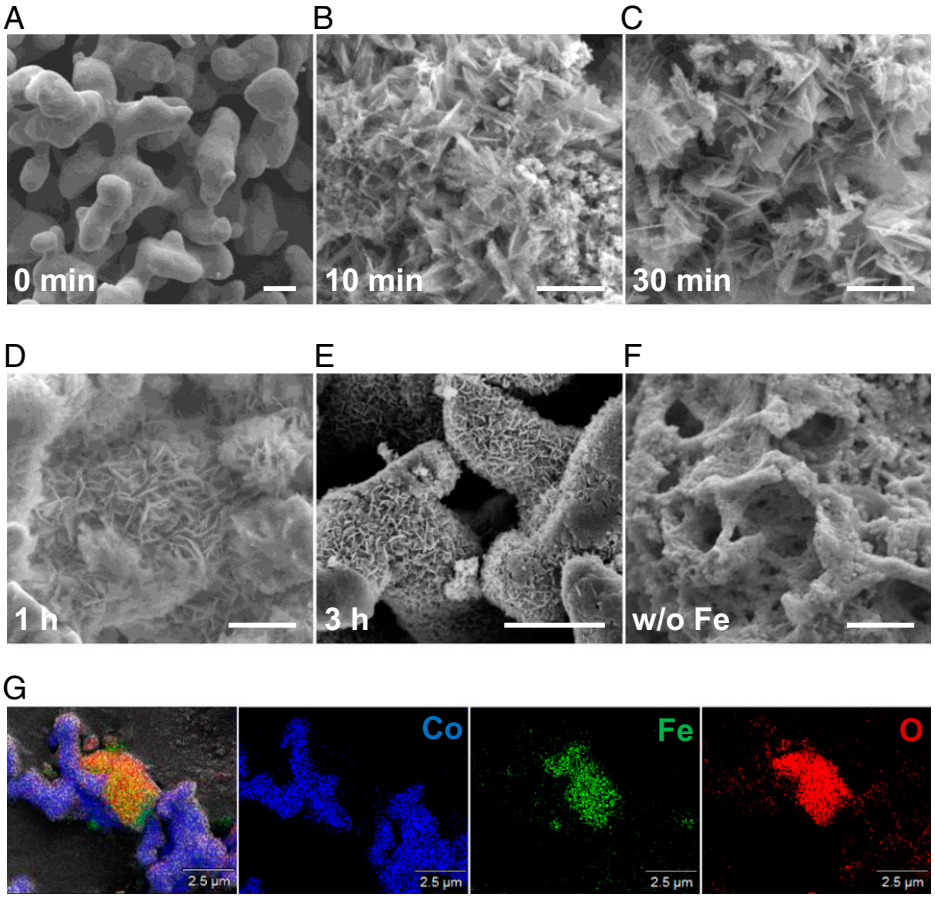

Fig. 3. Morphological evolution of Co in a hydrothermal environment. (*A*–*E*) Scanning electron microscopy (SEM) images of Co powder as a function of reaction time in the presence of Fe. Experimental conditions are the following: Fe, 80 mmol; $NaHCO_3$, 80 mmol; Co, 40 mmol; water filling, 50%; 300 °C, pH 8.23, 30 MPa. (*F*) SEM images of Co powder after reaction for 3 h without the addition of Fe. (Scale bars of *A*–*F*, 1 μm.) (*G*) Element mapping of the solid sample after reaction for 3 h.

peak of the vibration of bound HCO_3 located at 1,340 cm^{-1} was also observed both in the absence and presence of Co (*SI Appendix*, Fig. S19 and Fig. 4*A*). Second, the adsorbed HCO_3 is reduced to intermediate COOH, which then transfers to the Co surface, leading to the formation of Fe–OH groups, as evidenced by the cooccurrences of the Fe–OH peak at 3,676 cm^{-1} and the COOH peak at 1,390 cm^{-1}. The peak at 1,390 cm^{-1} can be assigned to the symmetric stretching mode of bound COOH on the Co surface (53), and this peak was not observed in the absence of Co. As mentioned before, the COOH intermediate prefers to adsorb on Co because of the higher-adsorption energy on Co (−2.28 eV) (51) than on FeO_x (−1.04 eV) (52), which suppresses the formation of $FeCO_3$. To confirm our assumption, we replaced Co with Ni and Cu, for which the adsorption energies of COOH are −2.25 and −1.52 eV (54), respectively. As expected, the formation of $FeCO_3$ was inhibited by increasing the adsorption energy of COOH on the metal surface (*SI Appendix*, Fig. S20), which further supported the transfer of COOH. Third, the bound COOH was reduced to CO, whose adsorption on Co is enhanced by Fe–OH to suppress the formation of $HCOO^-$. Finally, the adsorbed CO undergoes sequential reduction and further polymerizes into long-chain hydrocarbons.

Notably, based on the proposed pathway of C–C coupling, the HCO_3^- is not directly involved in the abiotic synthesis. The HCO_3^- first reacts with Fe to form $FeCO_3$, which either undergoes reductive decomposition into $HCOO^-$ or releases COOH to the Co surface. The proposed process is similar to the pathway that mantle-derived, inorganic carbon source takes rather than the one that seawater bicarbonate does, just as the former pathway has been shown to be directly responsible for the abiotic synthesis in an actual hydrothermal environment (2, 55, 56). Moreover, our system has both similar hydrothermal conditions and reaction pathways as those occurring in an actual hydrothermal environment, supporting the abiogenic origin of some hydrothermal petroleum.

Conclusions

In summary, our results show that hydrothermal reduction of $NaHCO_3$ can produce long-chain hydrocarbons up to $C_{24}H_{50}$ using general Fe and Co metals at ∼300 °C and 30 MPa. Bicarbonate is not only used as the carbon resource but also has a role of stabilizing Co, in which the honeycomb Co nanosheets are generated in situ. Operando ATR-FTIR revealed that the presence of Co promoted the formation of Fe–OH, which in turn enhanced the adsorption of the siderite-derived CO intermediate on Co for an efficient C–C coupling process. Taken together, we provide experimental evidence and insights into the mechanism of formation of long-chain hydrocarbons using native cobalt in the presence of Fe–OH in geologically feasible conditions on the early Earth. These findings may support the abiogenic hypothesis for some petroleum deposits, introduce an approach for nonnoble metal-catalyzed CO_2 conversion to petroleum fuel, and perhaps play into a better understanding of the emergence of life.

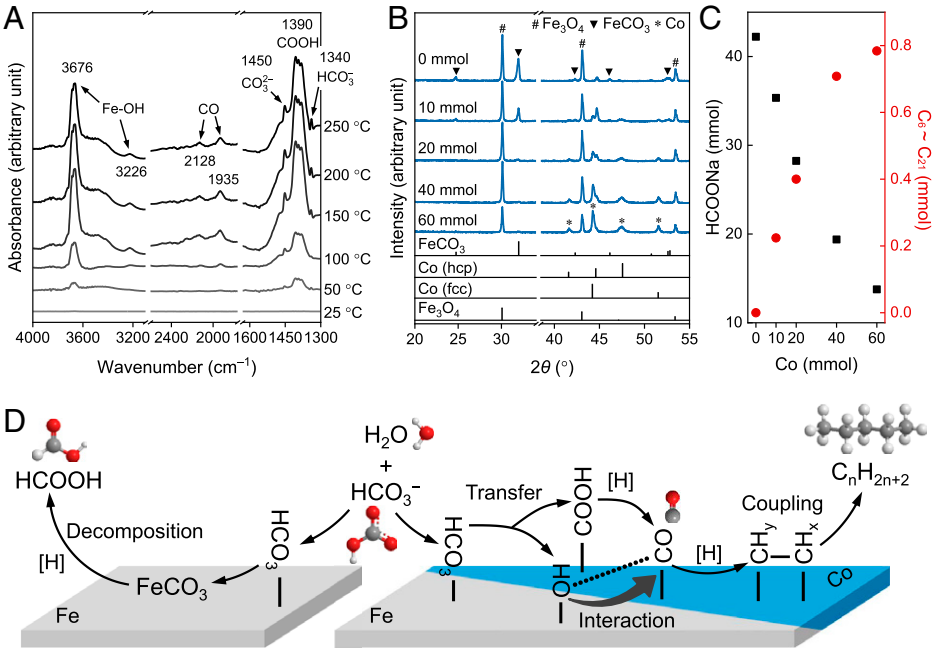

Fig. 4. Mechanism of $NaHCO_3$ reduction. (*A*) Operando ATR-FTIR spectra of $NaHCO_3$ reduction by Fe and Co metals. (*B* and *C*) XRD patterns of solid products (*B*) and the corresponding product distribution of HCOONa and long-chain hydrocarbons (*C*) as a function of initial Co amount. Experimental conditions are the following: Fe, 80 mmol; $NaHCO_3$, 80 mmol; water filling, 50%; 300 °C, 3 h, pH 8.23, 30 MPa. The vertical black lines in *B* are the XRD peaks of standard $FeCO_3$ (JCPDS No. 29–0696), Co (JCPDS No. 01–1278 for hcp and No. 15–0806 for fcc), and Fe_3O_4 (JCPDS No. 79–0418). (*D*) Proposed, competing pathways for the hydrothermal reduction of $NaHCO_3$ into $HCOO^-$ (*Left*) and long-chain hydrocarbons (*Right*). In the absence of Co, only $HCOO^-$ was formed by the reductive decomposition of $FeCO_3$. The addition of Co induced the transfer of the COOH intermediate accompanied by the generation of Fe−OH group, suppressing the formation of $FeCO_3$. The Fe−OH group enhanced the adsorption of CO, promoting the synthesis of long-chain hydrocarbons. JCPDS: Joint Committee on Powder Diffraction Standards.

Materials and Methods

Chemicals. Fe powder (325 mesh, ≥98%, Alfa Aesar Chemical Reagent), Co powder (≥99.9%, Sinopharm Chemical Reagent Co., Ltd; ≥99.9%, Aladdin Chemical Reagent; ≥99.8%, Alfa Chemical Reagent; ≥99.9%, Macklin Chemical Reagent), $NaHCO_3$ (AR, ≥99%, Sinopharm Chemical Reagent Co., Ltd), and H_2 (>99.995%, Shanghai Poly-Gas Technology Co.) were used.

Synthesis of Hydrocarbons. The synthesis of hydrocarbons was performed using a batch-type microautoclave (~42 cm^3) system, lined with SUS 316 stainless steel, and equipped with a high-pressure valve for collecting gas. In a typical run, Fe powder (80 mmol), $NaHCO_3$ (80 mmol), ultrapure water (20 mL, water-filling level of 50%), and Co powder (40 mmol) were added to the reaction chamber. The reactor was sealed and treated by heating the autoclave to 300 °C at a heating rate of 20 °C/min with constant shaking in an induced heating furnace. After the treatment, the autoclave was removed from the furnace and cooled with an air blower to room temperature. Water filling was defined as the ratio of the volume of the water put into the reactor to the inner volume of the reactor.

Detection of Organic Compounds. To detect the volatile hydrocarbons, the gas products were collected over a saturated NaCl solution and quantified by gas chromatography (GC) equipped with a thermal conductivity detector (Agilent GC7890A). To extract nonvolatile hydrocarbons, 5 mL dichloromethane (DCM) was injected into the reaction chamber after the reaction, and the reactor was shaken for 15 min. The DCM extract was analyzed by GC equipped with a mass spectrometry detector (Agilent GC7890A-MS5975C) for identification and a flame ionization detector (Agilent GC7890A) for quantification using an HP-5 column. The GC temperature program started at 35 °C for 5 min, ramped to 210 °C at 5 °C · min^{-1}, and was held at this temperature for 10 min. CO was confirmed by GC-MS with a molecular sieve column. The temperature program started at 35 °C for 2 min, ramped to 180 °C at 10 °C · min^{-1}, continued to ramp to 230 °C at 20 °C · min^{-1}, and was held at this temperature for 80 min. The organic acid anions in water were analyzed by GC-MS for identification and high-performance liquid chromatography (HPLC, Agilent 1260) for quantification. The GC-MS temperature program started at 40 °C for 4 min, ramped to 230 °C at 7 °C · min^{-1}, and was held at this temperature for 20 min. An Agilent 19091N-233HP-INNOWax Polyethylene Glyco column was used for sample separation. Helium (>99.999%) was used as the carrier gas. The HPLC was equipped with a tunable ultraviolet-visible detector adjusted at 210 nm and two Shodex RSpak KC-G columns. $HClO_4$ solution (2 mmol/L) was used as mobile phase with a flow rate of 0.8 mL/min.

Isotope Analysis. Carbon isotope ($\delta^{13}C$) and concentration analyses of CH_4, C_2H_6, and C_3H_8 were conducted on a gas chromatograph coupled with isotope ratio mass spectrometer (IRMS, DeltaplusXP, Thermo Fisher Scientific) via a combustion furnace and an open split interface (GC Combustion III, Thermo Fisher Scientific (57). Briefly, the experiment was carried out at the following conditions: injection temperature 250 °C; split ratio 5:1; flow rate 1.5 mL/min; oven temperature from 50 (maintained 5 min) to 150 °C (maintained 10 min) at a rate of 10 °C/min. Pure helium (>99.99995%) was used as the carrier gas by passing through an HP-PLOT-Q column (30 m × 0.32 mm internal diameter, 10-μm film thickness). After leaving the GC column, the separated gas subsequently entered a combustion furnace (operating at 960 °C) containing a ceramic tube packed with CuO, NiO, and Pt wires and transformed into CO_2, which was then analyzed by the IRMS. The carbon isotope ratios were calibrated by the simultaneous injections of a laboratory-working standard gas, which beforehand has been calibrated by the international standard. The precision of our $\delta^{13}C$ analysis is better than 0.5‰.

Catalyst Characterization. After DCM extraction, the reaction precipitate was washed with deionized water and dried in a vacuum oven at 60 °C for further characterization. XRD patterns were obtained on an SHIMADZU XRD-6100 PC with Cu Kα radiation (λ = 1.54184 Å) in steps of 0.02° and an accumulation time of 0.6 s per step at 40 kV and 40 mA. The peak identifications were carried out based on the reference patterns reported in the Power Diffraction File published by the International Centre for Diffraction Data. Scanning electron microscopy photographs were taken on a Hitachi s-4800 electron microscope at an acceleration voltage of 5 kV.

Operando ATR-FTIR. Operando ATR-FTIR was developed and performed to detect the intermediate in the $NaHCO_3$ reduction reaction. The spectra were recorded with a Nicolet FTIR spectrometer iS10 equipped with a liquid nitrogen–cooled, narrow-band mercury–cadmium–telluride detector and a

PC-50–300-DFIR high-pressure cell. The experiments were conducted at an elevated temperature from 25 to 250 °C. Spectra were collected as difference spectra, with the initial state as the background spectrum.

Data Availability. All study data are included in the article and/or *SI Appendix*.

ACKNOWLEDGMENTS. This work was supported by the National Key R&D Program of China (Grant Nos. 2018YFC0309800 and 2017YFC0506004), the State Key Program of Natural Science Foundation of China (Grant No. 21436007), the National Natural Science Foundation of China (Grant No. 21978170), the Natural Science Foundation of Shanghai (Grant No. 19ZR1424800), the Oceanic Interdisciplinary Program of Shanghai Jiao Tong University (Grant No. SL2020MS022), the Start-up Fund for Youngman Research at Shanghai Jiao Tong University (SJTU), and the Centre of Hydrogen Science, SJTU, China. We thank Naizhong Zhang for technique support of isotope measurement.

1. J. Horita, M. E. Berndt, Abiogenic methane formation and isotopic fractionation under hydrothermal conditions. *Science* **285**, 1055–1057 (1999).
2. G. Proskurowski *et al.*, Abiogenic hydrocarbon production at lost city hydrothermal field. *Science* **319**, 604–607 (2008).
3. A. Kolesnikov, V. G. Kutcherov, A. F. Goncharov, Methane-derived hydrocarbons produced under upper-mantle conditions. *Nat. Geosci.* **2**, 566–570 (2009).
4. M. J. Russell, W. Nitschke, E. Branscomb, The inevitable journey to being. *Philos. Trans. R. Soc. Lond. B Biol. Sci.* **368**, 20120254 (2013).
5. G. P. Glasby, Abiogenic origin of hydrocarbons: An historical overview. *Resour. Geol.* **56**, 83–96 (2006).
6. T. M. McCollom, J. S. Seewald, Abiotic synthesis of organic compounds in deep-sea hydrothermal environments. *Chem. Rev.* **107**, 382–401 (2007).
7. D. I. Foustoukos, W. E. Seyfried Jr., Hydrocarbons in hydrothermal vent fluids: The role of chromium-bearing catalysts. *Science* **304**, 1002–1005 (2004).
8. W. Martin, J. Baross, D. Kelley, M. J. Russell, Hydrothermal vents and the origin of life. *Nat. Rev. Microbiol.* **6**, 805–814 (2008).
9. S. J. Varma, K. B. Muchowska, P. Chatelain, J. Moran, Native iron reduces CO_2 to intermediates and end-products of the acetyl-CoA pathway. *Nat. Ecol. Evol.* **2**, 1019–1024 (2018).
10. K. B. Muchowska *et al.*, Metals promote sequences of the reverse Krebs cycle. *Nat. Ecol. Evol.* **1**, 1716–1721 (2017).
11. F. L. Sousa, M. Preiner, W. F. Martin, Native metals, electron bifurcation, and CO_2 reduction in early biochemical evolution. *Curr. Opin. Microbiol.* **43**, 77–83 (2018).
12. L. Daniels, N. Belay, B. S. Rajagopal, P. J. Weimer, Bacterial methanogenesis and growth from CO_2 with elemental iron as the sole source of electrons. *Science* **237**, 509–511 (1987).
13. S. Kato, I. Yumoto, Y. Kamagata, Isolation of acetogenic bacteria that induce biocorrosion by utilizing metallic iron as the sole electron donor. *Appl. Environ. Microbiol.* **81**, 67–73 (2015).
14. N. J. Tosca, C. Z. Jiang, B. Rasmussen, J. Muhling, Products of the iron cycle on the early Earth. *Free Radic. Biol. Med.* **140**, 138–153 (2019).
15. M. J. Russell, R. M. Daniel, A. J. Hall, J. A. Sherringham, A hydrothermally precipitated catalytic iron sulphide membrane as a first step toward life. *J. Mol. Evol.* **39**, 231–243 (1994).
16. M. W. Hitzman, A. A. Bookstrom, J. F. Slack, M. L. Zientek, "Cobalt—Styles of deposits and the search for primary deposits" (Open-File Rep. 53, Reston, VA, U.S. Geological Survey, 2017).
17. R. Sakai, Y. Kuroda, Native iron and the associated minerals from the ultramafic masses in the Sanbagawa belt, central Japan. *J. Jpn. Assoc. Miner. Petrol. Econ. Geol.* **78**, 467–478 (1983).
18. G. A. Challis, J. V. P. Long, Wairauite—A new cobalt-iron mineral. *Mineral. Mag.* **33**, 942–948 (1964).
19. R. Tao *et al.*, Formation of abiotic hydrocarbon from reduction of carbonate in subduction zones: Constraints from petrological observation and experimental simulation. *Geochim. Cosmochim. Acta* **239**, 390–408 (2018).
20. W. Zhou *et al.*, New horizon in C1 chemistry: Breaking the selectivity limitation in transformation of syngas and hydrogenation of CO_2 into hydrocarbon chemicals and fuels. *Chem. Soc. Rev.* **48**, 3193–3228 (2019).
21. K. D. Yang *et al.*, Morphology-directed selective production of ethylene or ethane from CO_2 on a Cu mesopore electrode. *Angew. Chem. Int. Ed. Engl.* **56**, 796–800 (2017).
22. L. Fan *et al.*, Strategies in catalysts and electrolyzer design for electrochemical CO_2 reduction toward C_{2+} products. *Sci. Adv.* **6**, eaay3111 (2020).
23. F. Jin *et al.*, High-yield reduction of carbon dioxide into formic acid by zero-valent metal/metal oxide redox cycles. *Energy Environ. Sci.* **4**, 881–884 (2011).
24. H. Zhong *et al.*, Selective conversion of carbon dioxide into methane with a 98% yield on an in situ formed Ni nanoparticle catalyst in water. *Chem. Eng. J.* **357**, 421–427 (2019).
25. A. K. Dalai, B. H. Davis, Fischer–Tropsch synthesis: A review of water effects on the performances of unsupported and supported Co catalysts. *Appl. Catal. A Gen.* **348**, 1–15 (2008).
26. R. W. Dorner, D. R. Hardy, F. W. Williams, H. D. Willauer, Heterogeneous catalytic CO_2 conversion to value-added hydrocarbons. *Energy Environ. Sci.* **3**, 884–890 (2010).
27. A. Y. Khodakov, W. Chu, P. Fongarland, Advances in the development of novel cobalt Fischer-Tropsch catalysts for synthesis of long-chain hydrocarbons and clean fuels. *Chem. Rev.* **107**, 1692–1744 (2007).
28. M. Wolf, N. Fischer, M. Claeys, Water-induced deactivation of cobalt-based Fischer–Tropsch catalysts. *Nat. Catal.* **3**, 962–965 (2020).
29. W.-Z. Li *et al.*, Chemical insights into the design and development of face-centered cubic ruthenium catalysts for Fischer-Tropsch synthesis. *J. Am. Chem. Soc.* **139**, 2267–2276 (2017).
30. Y. Xu *et al.*, Direct conversion of CO and H_2O into liquid fuels under mild conditions. *Nat. Commun.* **10**, 1389 (2019).
31. H. Wang *et al.*, Platinum-modulated cobalt nanocatalysts for low-temperature aqueous-phase Fischer-Tropsch synthesis. *J. Am. Chem. Soc.* **135**, 4149–4158 (2013).
32. Z. He *et al.*, Synthesis of liquid fuel via direct hydrogenation of CO_2. *Proc. Natl. Acad. Sci. U.S.A.* **116**, 12654–12659 (2019).
33. X. Wang *et al.*, In situ formed metal oxide/metal interface enhanced C–C coupling in CO_2 reduction into CH_3COOH over hexagonal closed-packed cobalt. *ACS Sustain. Chem. Eng.* **9**, 1203–1212 (2021).
34. D. A. Sverjensky, V. Stagno, F. Huang, Important role for organic carbon in subduction-zone fluids in the deep carbon cycle. *Nat. Geosci.* **7**, 909–913 (2014).
35. T. M. McCollom, Abiotic methane formation during experimental serpentinization of olivine. *Proc. Natl. Acad. Sci. U.S.A.* **113**, 13965–13970 (2016).
36. T. M. McCollom, B. S. Lollar, G. Lacrampe-Couloume, J. S. Seewald, The influence of carbon source on abiotic organic synthesis and carbon isotope fractionation under hydrothermal conditions. *Geochim. Cosmochim. Acta* **74**, 2717–2740 (2010).
37. T. M. McCollom, Laboratory simulations of abiotic hydrocarbon formation in Earth's deep subsurface. *Rev. Mineral. Geochem.* **75**, 467–494 (2013).
38. H. Ueda, T. Shibuya, Composition of the primordial ocean just after its formation: Constraints from the reactions between the primitive crust and a strongly acidic, CO_2-rich fluid at elevated temperatures and pressures. *Minerals (Basel)* **11**, 389 (2021).
39. J. M. Le *et al.*, Tuning mechanism through Buffer dependence of hydrogen evolution catalyzed by a cobalt mini-enzyme. *Biochemistry* **59**, 1289–1297 (2020).
40. B. Kandemir, L. Kubie, Y. Guo, B. Sheldon, K. L. Bren, Hydrogen evolution from water under aerobic conditions catalyzed by a cobalt ATCUN metallopeptide. *Inorg. Chem.* **55**, 1355–1357 (2016).
41. J.-W. Wang *et al.*, A molecular cobalt hydrogen evolution catalyst showing high activity and outstanding tolerance to CO and O_2. *Angew. Chem. Int. Ed. Engl.* **58**, 10923–10927 (2019).
42. J. Lin *et al.*, Remarkable effects of hydroxyl species on low-temperature CO (preferential) oxidation over $Ir/Fe(OH)_x$ catalyst. *J. Catal.* **319**, 142–149 (2014).
43. F. Solymosi, An infrared study of CO and NO adsorption on alumina-supported iridium catalyst. *J. Catal.* **62**, 253–263 (1980).
44. Y. Huang *et al.*, "Ir-in-ceria": A highly selective catalyst for preferential CO oxidation. *J. Catal.* **255**, 144–152 (2008).
45. R. Kefirov, E. Ivanova, K. Hadjiivanov, S. Dzwigaj, M. Che, FTIR characterization of Fe^{3+}–OH groups in Fe–H–BEA zeolite: Interaction with CO and NO. *Catal. Lett.* **125**, 209–214 (2008).
46. E. Ivanova *et al.*, Evidencing three distinct FeII sites in Fe–FER zeolites by using CO and NO as complementary IR probes. *Appl. Catal. B* **93**, 325–338 (2010).
47. W. Deng *et al.*, Crucial role of surface hydroxyls on the activity and stability in electrochemical CO_2 reduction. *J. Am. Chem. Soc.* **141**, 2911–2915 (2019).
48. K. W. Kimura *et al.*, Selective electrochemical CO_2 reduction during pulsed potential stems from dynamic interface. *ACS Catal.* **10**, 8632–8639 (2020).
49. S. Zhu, T. Li, W.-B. Cai, M. Shao, CO_2 electrochemical reduction as probed through infrared spectroscopy. *ACS Energy Lett.* **4**, 682–689 (2019).
50. V. P. Aguirre *et al.*, Synthesis and characterization of mixed-valent iron layered double hydroxides ("green rust"). *ACS Earth Space Chem.* **5**, 40–54 (2020).
51. S. Lin, J. Huang, X. Gao, X. Ye, H. Guo, Theoretical insight into the reaction mechanism of ethanol steam reforming on Co(0001). *J. Phys. Chem. C* **119**, 2680–2691 (2015).
52. L. Huang, B. Han, Q. Zhang, M. Fan, H. Cheng, Mechanistic study on water gas shift reaction on the Fe_3O_4 (111) reconstructed surface. *J. Phys. Chem. C* **119**, 28934–28945 (2015).
53. N. J. Firet, W. A. Smith, Probing the reaction mechanism of CO_2 electroreduction over Ag films via operando infrared spectroscopy. *ACS Catal.* **7**, 606–612 (2016).
54. J. A. Herron, J. Scaranto, P. Ferrin, S. Li, M. Mavrikakis, Trends in formic acid decomposition on model transition metal surfaces: A density functional theory study. *ACS Catal.* **4**, 4434–4445 (2014).
55. J. M. McDermott, J. S. Seewald, C. R. German, S. P. Sylva, Pathways for abiotic organic synthesis at submarine hydrothermal fields. *Proc. Natl. Acad. Sci. U.S.A.* **112**, 7668–7672 (2015).
56. S. Q. Lang *et al.*, Deeply-sourced formate fuels sulfate reducers but not methanogens at Lost City hydrothermal field. *Sci. Rep.* **8**, 755 (2018).
57. A. Gilbert, K. Yamada, K. Suda, Y. Ueno, N. Yoshida, Measurement of position-specific 13C isotopic composition of propane at the nanomole level. *Geochim. Cosmochim. Acta* **177**, 205–216 (2016).